DOI: 10.13009/EUCASS2023-507
Aerospace Europe Conference 2023 – 10TH EUCASS – 9TH CEAS

DNS investigation of turbulent flows in rectangular smooth and rough ducts

T. Santese[*1], D. Sanchis*[1]*, A. Sternin*[1]*, C. Manfletti*[1]

[1]Technical University of Munich, Germany;
TUM School of Engineering and Design, Department of Aerospace and Geodesy

Abstract

Rocket engine performance and durability rely heavily on efficient cooling systems to manage extreme heat generated during operation. Understanding the complex interplay between friction effects and heat transfer phenomena is crucial for optimizing cooling channel designs, whose freedom is now enhanced by new techniques of additive manufacturing. In this study, we investigate the friction and heat transfer characteristics in rectangular cooling channels typical of rocket engines by using Direct Numerical Simulations (DNS) and comparing a smooth duct against one featuring a rough surface, emulated through riblets.

Our results reveal that the rectangular section significantly influences the flow patterns within the duct, generating secondary motions near the corners; furthermore, we emphasize the significance of surface roughness effects on overall heat transfer performance. The riblets influence the flow patterns, alter the velocity profiles, and enhance heat transfer and friction resistance compared to the smooth case.

1. Introduction

Regenerative cooling in liquid rocket engines has been widely used in the last decades because of the high thermal efficiency that can be reached by letting the propellant flow in cooling channels around the thrust chamber, and absorbing the power released by the combustion. In addition, that power can be employed as input power to operate turbomachinery.

The design process of the cooling channels has to consider the challenging operating conditions that have to be fulfilled and tries to optimize the performance of the overall thermal system, also accounting for system limitations or constraints, such as a prescribed outlet pressure, a maximum outlet temperature, or a minimum enthalpy intake, in the case of an expander cycle. The shape of the channels will dictate the thermal and frictional behavior of the coolant; thus, it is subject to careful analysis and design for which the development of new additive manufacturing technologies is of paramount importance. The enhanced freedom in the optimization process, which outputs the shape of the cooling channels, allows higher overall performances of the thermal system and power management of the rocket itself. However, the additive manufacturing process causes a much higher roughness of the surfaces with respect to traditional techniques, whose effects have to be predicted because of the significant change in fluid pattern, of momentum and of heat transfer near the rough wall; this alteration, if not correctly predicted, may lead to performance degradation and potentially catastrophic engine failure. Therefore, understanding the effects of surface roughness on heat transfer and fluid flow in rocket engine cooling channels is critical for developing reliable and high-performance rocket engines.

One of the earliest approaches to model surface roughness in fluid mechanics was introduced by Nikuradse in the 1930s, [26]. Nikuradse performed experiments in smooth pipes covered with sandpaper, whose roughness was well characterized by small spheres of a precise diameter, k_s. By running many experiments on pipes with different roughness sizes and different Reynolds numbers, Nikuradse studied the frictional behavior of the flow and presented three different roughness regimes, which were defined as: “hydrodynamically smooth”, “transitionally rough” and “fully rough”. In the first regime, the Reynolds number is very low and the roughness does not alter the friction factor; in the transitional regime both the Reynolds number and roughness dimension affect the flow, and in the last regime, at Reynolds number sufficiently high, the Reynolds number stops influencing the flow and the roughness dimension is the only important

DOI: 10.13009/EUCASS2023-507

parameter to determine the momentum losses of the flow. He also showed that the logarithmic-law of the wall still applies, with a downward shift to be additionally considered in case of a rough wall, Eq. (1).

$$u^+ = \frac{1}{k}\, ln(y^+) + B - \Delta U^+ \qquad with \qquad \Delta U^+ = B - 8.48 + \frac{1}{k}\, ln\left({k_s}^+\right) \tag{1}$$

Where k is the von Karman constant, equal to 0.41, B is the intercept for a smooth wall, and the + is used to indicate viscous scaling. ΔU^+ is commonly referred to as "roughness function" and Nikuradse proposed a logarithmic relation with the ${k_s}^+$, as in Eq. (1), where ${k_s}^+$ is known as "roughness Reynolds number" and is defined as ${k_s}^+ = k_s u_\tau / \nu$. Based on this, work Schlichting defined in [34] the well-known approach of "sand-grain roughness". This method relies on an experimental test of the rough surface, which allows us to define the frictional behavior of the specimen and then retrieve the corresponding sand-paper diameter whose frictional effect is the same. The sand-grain parameter is again indicated as k_s, and allows to use the Eq. (1) to predict the fluid behavior of the rough surface by means of one single parameter. Due to the complexity of the problem, it is worth it to recall that k_s is a flow property and not a fluid property, thus, an experimental test is required to retrieve the sand-grain parameter at different operating conditions. Nevertheless, there were many attempts to find direct correlations between the geometrical features of the rough surface and this parameter, to have a prediction "a priori" of such parameter; the most common correlations were gathered and carefully compared in [8], and are still active research topic as can be seen in [13]. These correlations attempt to relate the most common statistical parameters used when dealing with rough surfaces with the sand grain parameter.

The research for correlations which help the description of the modifications of the flow induced by surface roughness, has been enhanced by the increase in computational resources of the last decades, which have allowed to perform DNS and study in detail the modification of the velocity profile and many other quantities which are not measurable in experiments. Especially the development of RANS (Reynolds Averaged Navier-Stokes) models can benefit of the deep knowledge derived from DNS results, which can explain the physics behind some phenomena. For example, Spalart [36], was capable of deriving a constitutive relation for the Reynolds Stress Tensor, which considers its anisotropy, substantially improving the results from any model using the Boussinesq assumption.
Discrete roughness elements have often been used in these simulations to reproduce the flow alteration in a simple way, respecting the statistical parameters which describe real rough surfaces. In particular, riblets, cubes, and spheres have been implemented; a few examples are [6, 16, 21, 22, 24, 27, 28]. Less works reported realistic roughness obtained by scanning real components [4, 5, 9, 38]. This is because the scanning process may introduce difficult-to-resolve wavelengths of the surface, as explained in [4], in which a low-pass filter was used in order to overcome this problem.
In addition, when dealing with rough surfaces most of the works focused on understanding the friction behavior of the fluid. Little or no attention has been paid to the enhancement of the heat transfer near the wall. [22] is one of the first DNS reports involving heat transfer on a rough wall, and riblets were implemented to replicate roughness. A similar setup was used in other works [24][28]. Heat transfer on realistic surfaces is even more difficult to find in literature, and the only example known to the author is [9]. In this work, a rough surface is extracted from microscopy of a combustion chamber deposits, and DNS is used to estimate an average friction factor and an average Nusselt number over the rough wall. It is commonly understood that surface roughness increases both the friction factor of the flow and the heat transfer on the wall, however, the two phenomena are not enhanced in the same way, and studies have been focusing on the relative increase of these two. It is usual to describe the frictional behavior of the flow utilizing the skin friction Cf and the heat transfer utilizing of the Stanton number, St, or the Nusselt number, Nu. In [1], experimental data in a low-speed wind tunnel are gathered at various flow conditions and Reynold number to propose a suitable "Reynold analogy factor" in order to estimate the relative increase of friction factor with respect to heat transfer coefficient; they defined $RA = 2St/C_f$, and showed that the momentum transfer is more enhanced with respect to the heat transfer and that RA usually assumes values between 0.5 and 0.7.

In order to apply this research to cooling channel applications, another essential factor to be considered is the presence of side walls. Indeed, when simulating a turbulent channel flow, periodic boundary conditions are frequently used on the side walls, as can be seen in almost all the DNS works which have been cited up to now; this procedure allows to easier considerably the post-processing of the data because it becomes possible to neglect one spatial direction and the effect of the side walls on the fluid. Plus, the averaging process can be carried out in the spanwise direction, which greatly reduces the amount of data to be simulated, thus reducing the duration of the simulation and the computational cost. However, the presence of the side-walls is heavily influencing the flow because of the side boundary layer and the interaction between core flow and near-wall flow, which creates secondary motion near the corners; secondary flow motions near the four corners of the duct have been studied in previous works [30, 32], and are indicators of non-zero stream-wise vorticity which in turns is caused by a Reynolds stress gradient near the corner (only present for non-circular cross sections). In square ducts [30], secondary motions come in the form of 8 counter-rotating vortices, bringing fluid from the high-momentum region in the core section to the wall corners. The intensity of these currents is in the order of 1-2% of the bulk velocity, but this relationship has been studied at different flow conditions: in [2], it was found that secondary flows should not be affected by the Reynolds number. However it is stated in [12] that the intensity of the secondary eddies can be expressed as a percentage of the bulk velocity and decreases with increasing Reynolds number. The first DNS simulation of a square duct is recalled to be the one from Gavrilakis [11], using a bulk Reynolds number of 4410. Higher Reynolds numbers were simulated in [40, 43], and more recently in [23, 30, 44]. In the last two works, the relation with the Reynolds number was further analyzed by creating a wide database ranging from Reynolds number of 4.000 to 40.000. Rectangular ducts and the effect of the aspect ratio (AR) of the channel were investigated in [40, 41], where aspect ratios up to 7 have been analyzed, resulting in a friction factor initially increasing with AR, then decreasing again after AR > 3; heat transfer was not included in any of these works.

This paper aims to contribute to the ongoing research on surface roughness; DNS simulations of turbulent flow in rectangular ducts, with heat transfer and discrete riblets on the hot wall, have been performed and compared to the results of a smooth wall. The simulation setup is similar to the one used in [24] and [9], but periodic boundary conditions on the side walls are not used, and the side walls are simulated through a non-slip condition. This paper investigates the influence of the rough surface, simulated through the use of riblets, on the flow development in a rectangular duct and we present the variation of the friction factor and the Nusselt number with respect to a smooth case. As far as the author acknowledges, this is the first research accounting for a duct flow with roughness.

2. Numerical Procedure

The compressible turbulent flow has been solved with the EBI-DNS code [45–47], based on the open-source code OpenFOAM [42] . The code is initially developed for reacting flows and then modified in order to switch the reactive mechanism off and simulate the fluid in cooling channels as a non-reactive flow. This choice has been made because the solver has been widely used in our research group [17, 18, 20, 37], and although it is thought for reactive flows, it can be easily modified to simulate non-combustion-related problems; plus, this gives us the flexibility to investigate thermal cracking of hydrocarbons in the future, [10]. The set of Navier-Stokes equation is solved as reported in Eq. 5-7.

$$\frac{\partial \rho}{\partial t} + \nabla \cdot (\rho \mathbf{U}) = 0 \tag{5}$$

$$\frac{\partial (\rho \mathbf{U})}{\partial t} + \nabla \cdot (\rho \boldsymbol{U}\boldsymbol{U}) = -\nabla p + \nabla \cdot \left(\mu \left(\nabla \boldsymbol{U} + (\nabla \boldsymbol{U})^T - \frac{2}{3} \overline{\overline{I}}\, \nabla \cdot \boldsymbol{U} \right) \right) \tag{6}$$

$$\frac{\partial \left(\rho \left(h_s + \frac{1}{2} \mathbf{U} \cdot \mathbf{U} \right) \right)}{\partial t} + \nabla \cdot \left(\rho \mathbf{U} \left(h_s + \frac{1}{2} \mathbf{U} \cdot \mathbf{U} \right) \right) = -\boldsymbol{\nabla} \cdot \mathbf{q} + \frac{\partial p}{\partial t} \tag{7}$$

With $-\boldsymbol{\nabla} \cdot \mathbf{q} = \boldsymbol{\nabla} \cdot \left(\frac{\lambda}{c_p} \boldsymbol{\nabla} h \right)$

In this paper, $\mathbf{U}$ is the velocity vector**,** ρ the density, p the pressure, λ the thermal conductivity, c_p the isobaric heat capacity and μ the molecular viscosity. The energy equation is formulated as a function of the sensible enthalpy, which for ideal gases can be defined as $h_s = h - h_o$, where h_o is the enthalpy of formation of the specie. In this set of equations, viscous work $\nabla \cdot (\tau \cdot u)$, potential energy, radiation and Dufour effect are neglected. The equations are solved in OpenFOAM using the well-known PIMPLE algorithm. For more information on the solver see [47] . An inlet velocity boundary condition is applied to ensure mass flow consistency and obtain the desired bulk Reynolds number. Periodic synthetic turbulence is generated with the scheme described in [19], based on the strategy proposed by Shur et al in [35]. proposed by Kraichnan [15]. The synthetically generated velocity field develops with enough length to ensure

DOI: 10.13009/EUCASS2023-507

convergence into a mature turbulent flow; this turbulence has been added at the inlet of the channels in order to save computational time for the transition of the flow from laminar to turbulent. The detailed process is explained and validated in [19], and further used in [17, 18, 20, 37].

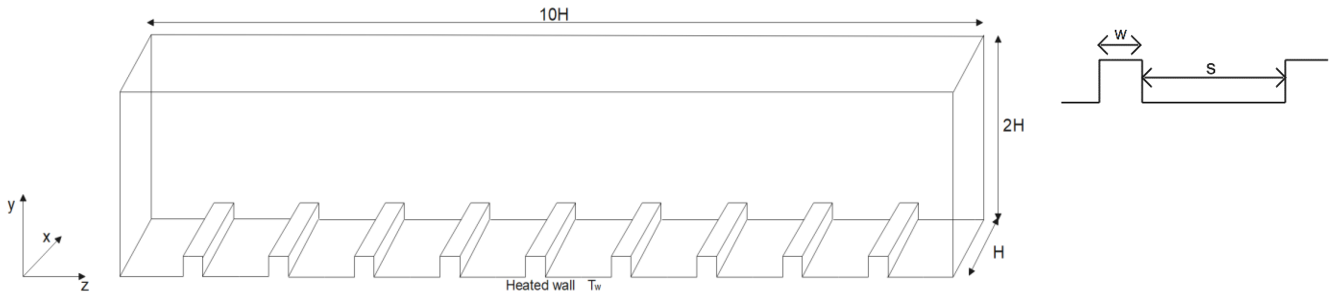

Figure 1 Simulation domain.

The simulated domain is shown in Fig. 1. A rectangular channel is considered with an aspect ratio of 2 and L = 20H, being H the half-channel height. The length of the channel has been chosen accordingly to previous studies, in which iterative procedures were undertaken to understand how much space is needed to develop the flow fully; for reference, a length of $4\pi H$ was used in [29], $6\pi H$ in [30], $25H$ in [40], similarly to what was done in [11].
The riblets are square with height w and spacing s between each other; in this study we considered $s = 0.85H$ and $w = 0.15$; these values have been chosen to resemble the average statistics (mean roughness height and peak-to-valley height) of additively manufactured through laser beam melting (LBM) processes.
These values have been chosen because of a future interest in scanning the surface of interest and performing DNS on the scanned sample; this will allow us to compare the results between two different simulations whose rough walls have similar statistical descriptions.
As already mentioned, in previous literature work [3–5, 9, 24, 28], the side walls of the channels were not simulated and periodic boundary conditions were used; in this study, the secondary flows which arise in the corner of the rectangular section and provide an enhancement of the mixing and thus of the heat flux, are one of the most significant aspects to be studied. For this reason, here, the side walls are simulated through no-slip boundary conditions. The geometry of the domain has been fixed as in Fig.1, and two simulations have been performed, one with a smooth bottom wall and one with equally spaced squared riblets on the bottom wall.

3. Convergence of the simulation and error estimation

Time integration is performed with a 2nd order Runge-Kutta scheme, and temporal averaging is performed using Favre-averaging [7], which has been considered more suitable to the case due to the density variation near the wall. As said, secondary motions are usually characterized by a velocity in order to 2% of the bulk velocity; thus their weak intensity requires very long averaging time to get reasonable convergence of the flow statistics, as first observed in [29, 39]; the convergence of the simulation has been judged based on a symmetric-indicator used in [30] which define how symmetric the flow is concerning the expected symmetry among the four quadrants, Eq.8.

$$\varepsilon_s = \frac{1}{U_b}\left[\frac{1}{H^2}\int_0^{2H}\int_0^{H}\left(\bar{u}(x,y) - \overline{u_{sym}}(x,y)\right)^2 dxdy\right]^{0.5} \tag{8}$$

Where $\overline{u_{sym}}(y,z)$ is the mean velocity averaged over the two vertical halves of the duct. In this way, the time-averaging interval can considered long enough to get the statistical properties to be symmetric along the vertical direction of the duct. A remarkable analysis of the convergence criteria to establish the convergence of duct-flow simulation has been carried out in [41], where it is suggested to average over an approximate interval of 200 convective times to get their convergence indicator down to a value of 10^{-3}, with the convective time defined as H/U_b. The bulk Reynolds number,

DOI: 10.13009/EUCASS2023-507

Re_b, the friction Reynolds number Re_τ, the number of cells used and the convergence indicator are reported in Tab.1, along with some other quantities resulting from each simulation.

Table 1 Simulation details.

Simulation	Re_b	Re_τ	N_x	N_y	N_z	Δt_{conv}	ε_s	Δx / η
Smooth	6700	~230	120	240	1200	120	2.1e-2	0.93
Riblet	6400	~230	140	280	1400	100	1.0e-2	0.79

The simulations were run on fine meshes in order to satisfy the requirements given by the Kolmogorov length, $\eta = \left(\frac{\nu}{\epsilon}\right)^{0.75}$, [31], with ν being the kinematic viscosity, ϵ the turbulent dissipation. Tab.1 reports the ratio between resolution Δx and Kolmogorov length η;

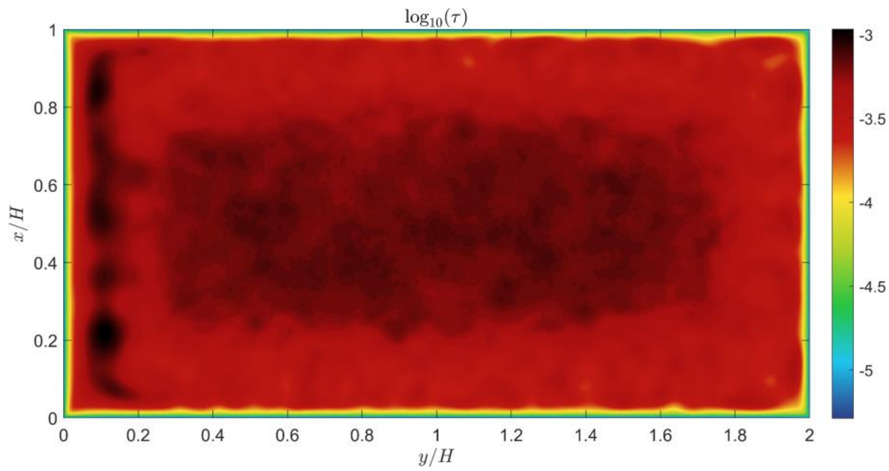

Figure 2 Turbulent time scale for the smooth duct simulation.

the Kolmogorov criteria has been successfully satisfied in the 98.7% of the cells, namely the smallest dimension of the eddies could be resolved in this simulation, and the average value of the ratio between the resolution and the Kolmogorov scale is found in the Tab.1 to be well below the threshold of 2.1, [31]. Regarding the time-convergence, the simulation time does not satisfy the suggested convergence criteria of [41], since the simulation is run for slightly more than 100 convective time steps, which means the flow statistics may not be accurately solved. In order to understand our limitations, the turbulence time scale has been evaluated, as $\tau = \left(\frac{k}{\epsilon}\right)$ and presented in Fig.2 for the smooth channel case. This parameter indicated the time interval which is necessary to have an independent measurement of the statistics of the flow [31]; this means that for the given time interval for which the simulations have been run, there will be more independent measurements and thus better-averaged statistics in the near wall region, where the turbulent time scale is smaller, and less measurement in the core region. From this analysis, we understand that we are not able to evaluate the statistics of the flow in the core region and in the darker part at $y/H = 0.1 - 0.2$, but we can focus our investigation on near-wall quantities. Indeed, the attention will mainly be paid to the wall shear stress, which decides the friction behavior of the flow and the temperature gradient on the wall, representing the heat transfer capabilities of the flow.

This said, we quantify the error which affects our simulations, and to do so, a stochastic approach is deemed suitable due to the chaotic nature of the turbulent flows. The Favre average we have adopted allows us to find a time-averaged value, $\bar{q}$, for every property of interest, thus evaluating the fluctuation at each timestep with respect to the expected value. Fluctuations around the average are essential parameters in turbulent flows and we need to quantify them; since the average over time of every fluctuation is zero, the second order moment, or variance, is commonly used. When averaging in time, because of the impossibility of averaging over infinite time interval, we introduce an error, $\bar{q}_e$, as in Eq.9.

DOI: 10.13009/EUCASS2023-507

$$\bar{q}^* = \frac{\sum q(t_i)\rho(t_i)}{\sum \rho(t_i)} = \bar{q} + \bar{q}_e \tag{9}$$

Assuming that the error has a Gaussian distribution and taking n_p independent measurements, it is possible to estimate the probability that the error overcomes a certain threshold α. The confidence interval $CI = 1 - \alpha$ indicates the probability of the error staying below the defined threshold, and it is often considered to be 95%, corresponding to an error of 5%. As already done in [17], we evaluate the number of independent measurements making use of the turbulent rate of dissipation and turbulent kinetic energy, as in Eq.10, and then we evaluate the associated error in a confidence interval of the 95% as in Eq.11.

$$n_p = \frac{2t_{sim}\bar{\epsilon}}{\bar{k}} \tag{10}$$

$$err_{CI} = \frac{t_{value}\ \sigma}{\sqrt{(n_p)}} \tag{11}$$

Where, t_{value} has been assumed 0.35 as in [17], which is a conservative approach, and σ is the standard variation (square root of the variance) of the interested quantity. The most relevant fluctuations in turbulent flows are those of the velocity field, mainly characterized by their variance, which defines the turbulent kinetic energy (TKE). Tab.2 reports the obtained errors in a CI of 95% for the velocity field, averaged on the simulation domain and made dimensionless.

Table 2 Error affecting the velocity field, in a CI = 95%, evaluated as $err_{CI}\ /\ \bar{q}\ * 100$.

U_x	U_y	U_z
17.6 %	12.8 %	0.25 %

It can be seen in Tab.2 that the error for the spanwise and wall-normal directions of the velocity vector is much higher with respect to the error in the streamwise direction. The reason for this is the poor convergence in the core region of the duct, as explained before; however, it must be considered that the time-averaged magnitude of the x and y component of the velocity vector is in the order of $10^{-2} m/s$, thus, the absolute error is negligible for the analysis we carry out in the following sections.

4. Smooth Channel

This chapter presents the simulation results of a smooth rectangular channel, which is used as a reference to compare the effect of riblets. The streamwise component of the velocity vector is presented in Fig. 3, at a generic instant of time and after averaging; as expected, the instantaneous velocity field shows significant deviations with respect the averaged state, with the formation of small and large eddies which bring low momentum fluid into the core region and high-velocity fluid nearer to the walls. Peaks of velocity up to 20% higher than the bulk velocity are found in the core region, and especially at $y/H = 0.2 - 0.4$, where the density gradient plays a dominating role.

$$C_f = \frac{2\overline{\tau_w}}{\rho U_b^2} \qquad with \qquad U_b = \int_A \rho U \ / \int_A \rho \tag{9}$$

$$\tau_w = \mu \frac{dU_z}{dy} \tag{10}$$

DOI: 10.13009/EUCASS2023-507

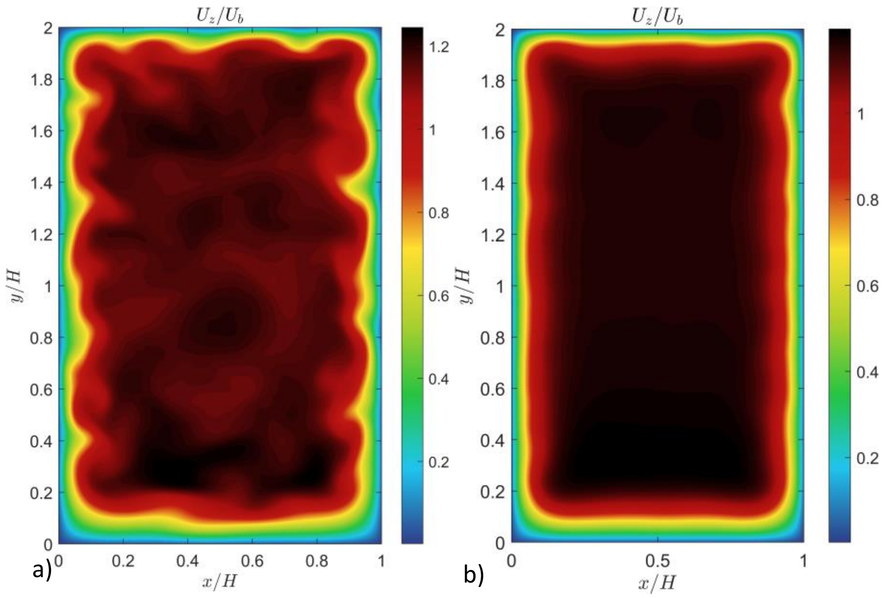

Figure 3 Streamwise velocity adimensionalized with respect to the bulk velocity a) at a generic instant of time b) averaged in time.

The evaluation of the skin friction coefficient and the Nusselt number has been carried out using time-averaged quantities, using the same mathematical procedure adopted in [25], namely averaging the properties on the perimeter of the section to extrapolate one single value for both the skin friction coefficient and the heat transfer coefficient, Eq.(9-10). Fig. 4 shows the skin friction coefficient obtained on the four walls.

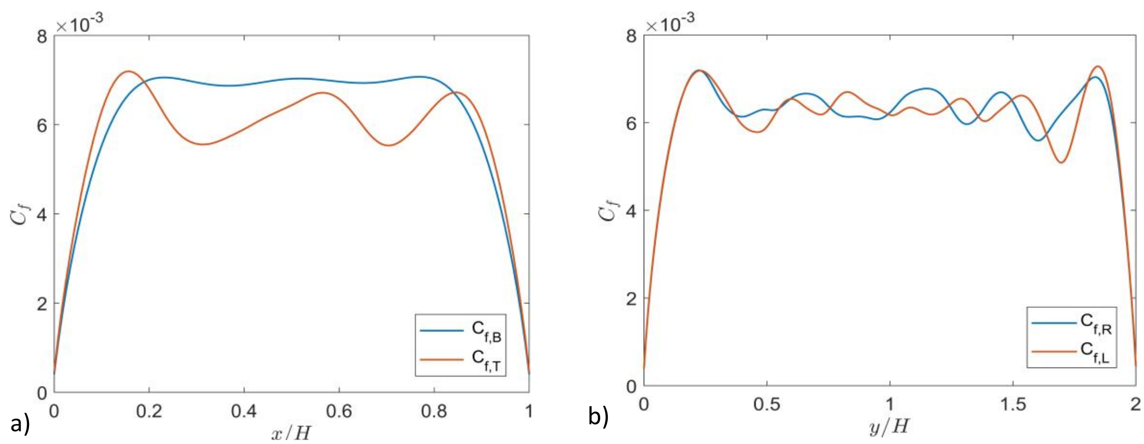

Figure 4 Skin friction coefficient for the four walls of the smooth duct. The subscripts "B,T,L,R" are used for the quantities over the "Bottom, Top, Left and Right" wall, respectively, looking at the inlet.

All four profiles show peaks near the corners, while oscillating around a constant value when moving away from the corners. However, it has to be noticed that: on the right and left walls, the fluctuations are very similar and keep an amplitude reasonably small, except for the two prominent peaks near the corners we mentioned before. It is instead noticeable the difference of the skin friction profile on the top and bottom walls; on the bottom wall, where the heat transfer process occurs, the density diminishes, the Reynolds number decreases, and the velocity and thermal boundary layer becomes thicker.

DOI: 10.13009/EUCASS2023-507

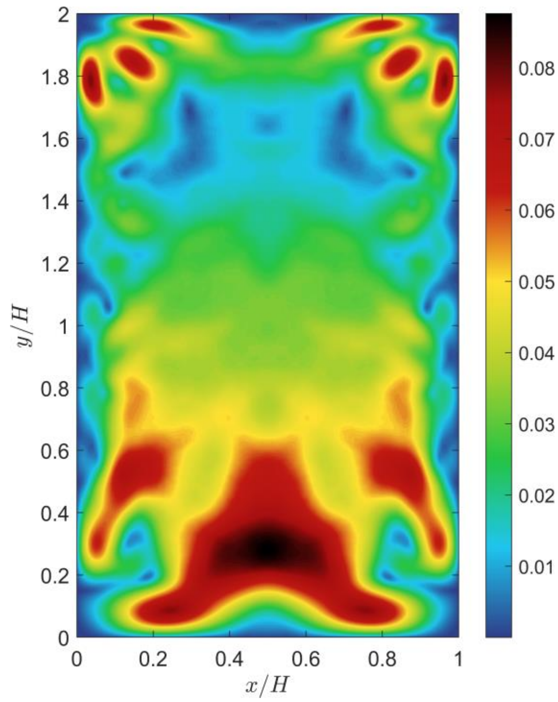

Figure 5 Cross-flow velocity $\left(U_x{}^2 + U_y{}^2\right)^{0.5}$ *presented on a cross section of the smooth duct*

The slower change in properties helps in smoothening the skin friction profile, or more in general, to get flow statistics, which are easier to average. On the top wall, instead, no heat transfer occurs, the density is higher, and the velocity boundary layer is thinner, which makes it more challenging to get adequately averaged statistics. In addition, an interesting phenomenon that can be observed and helps explain the oscillating behavior on the top wall is the cross-flow velocity assessment, which gives rise to secondary flow structures. Fig. 5 presents the cross-flow velocity defined as $\left(\mathrm{U_x}{}^2 + \mathrm{U_y}{}^2\right)^{0.5}$ which is also used in [40] as the main indicator for the presence of secondary flows. On the top wall, secondary flows are very clearly visible near the corners, the identical three counter-rotating vortices as presented in [40], in which a similar friction Reynolds number was used. These vortices have a magnitude of less than 2% of the bulk velocity; however, they affect the global structure of the flow in the near wall region and in the core region, moving high-momentum flow from the core region to the walls.

On the bottom wall, vortices can still be recognized near the corners; however, their structure is absorbed in a mor significant fluid motion, which is due to the heating process and the following density decrease; the lighter fluid tends to go up, creating a significant current in the center plane, whose magnitude is very comparable to the secondary flows on the top, but affects a much larger area of the domain. It is crucial to notice that even if these motions have comparable magnitude, their nature is very different: the vortices on the top are created by anisotropy of the Reynolds stress tensor near the wall, while the rising current on the bottom of the channel is due to the heating process and the consequent thermodynamic variation inside the fluid. As explained in the previous chapter, a thorough convergence of the statics was not reached in these simulations, thus a quantitative assessment of the intensity of these secondary flows will not be carried out here. Nonetheless, Fig.5 helps in explaining the oscillating behavior of the skin friction coefficient on the top wall; indeed, the bottom wall presents a near-wall region less affected by cross-flow velocity, which has a thick gradient on the wall, and gets stronger only at $y/H = 0.05\text{–}\,0.1$, thus the wall shear stress on the wall is not primarily influenced by these motions. On the contrary, the top wall presents vortices at a coordinate $x/H = 0.2$ and $x/H = 0.8$ which are pushed to the wall and whose intensities is large enough in the very near wall area to influence the wall shear stress in that region; indeed, two valleys are visible in Fig. 4a on exactly those x-coordinates.

For what concerns the heat transfer process occurring on the wall, the Nusselt number has been used to characterize the process. The Nusselt number is defined as in Eq. 11, where the characteristic length has to take into account the

DOI: 10.13009/EUCASS2023-507

asymmetry of the flow and that just one of the walls is being heated; thus, a value of four times the half channel height is used, as was done in [9].

$$Nu = \frac{h * 4H}{\lambda} \qquad h = \frac{\lambda \frac{dT}{dy}|_{y=0}}{T_w - T_b} \tag{11}$$

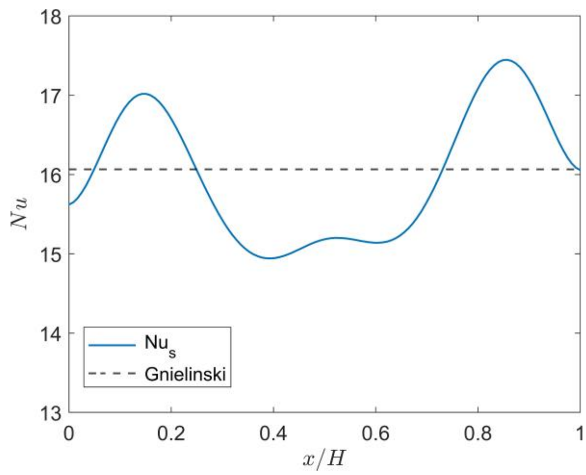

Figure 6 Nusselt number on the heated wall of the smooth duct (continuous line) and Gnielinski correlation (dashed line).

Here, the h_s is the heat transfer coefficient on the heated wall, while the bulk temperature T_b has been evaluated as $\int_A T \rho U dA / \int_A \rho U dA$. The resulting Nusselt number on the bottom wall is reported in Fig. 6, along with an empirical reference. The good agreement with the Gnielinski correlation, [33], in which the Prandtl number, the Reynold number and the derived friction factor of our simulation have been used, confirms the correct choice of taking an adapted characteristic length. In addition, two evident peaks are visible near the corners, approximatively at the same x-coordinate where large vortices can be distinguished in Fig. 5.

5. Rough Channel

In order to keep the comparison between the two simulations reliable, the post evaluation of the quantities is carried out in the same way, with minor differences due to the complex geometry and flow field, which has to be analyzed. Most importantly, it has been noticed that the velocity field becomes periodic over the repetition of a riblet and a smooth space. Thus, we focus on one repetition of this periodic geometry and highlight the different velocity and thermal fields, not only by comparing the riblet and the following space but also by what happens on the side walls over the riblet and the spacing. In a first analysis, Fig. 7 presents the velocity field in a generic timestep, Fig.7a, and averaged in time, Fig. 7b, in a section of the channel that does not cut any riblet. The main difference with respect to the previous case is evident on the bottom: a thicker boundary layer is visible which is created by the interaction between the fluid and the rough wall; in particular negative values are visible on the very bottom (in blue) which are due to heavy recirculation zone between riblets, characteristic of k-type roughness [14], which are highlighted in Fig.8.

DOI: 10.13009/EUCASS2023-507

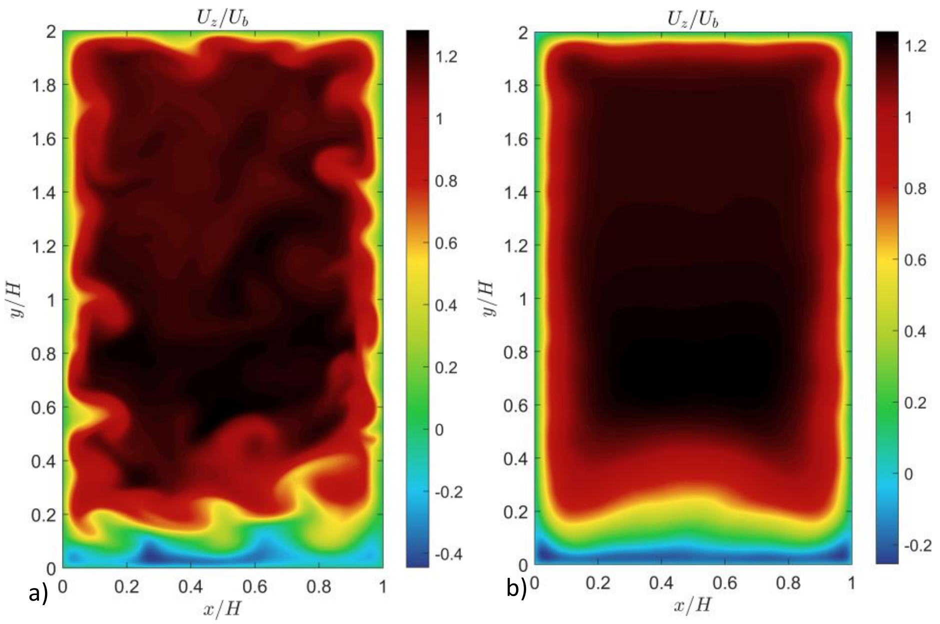

Figure 7 Velocity field in a section with no riblets a) in a generic instant of time b) averaged in time

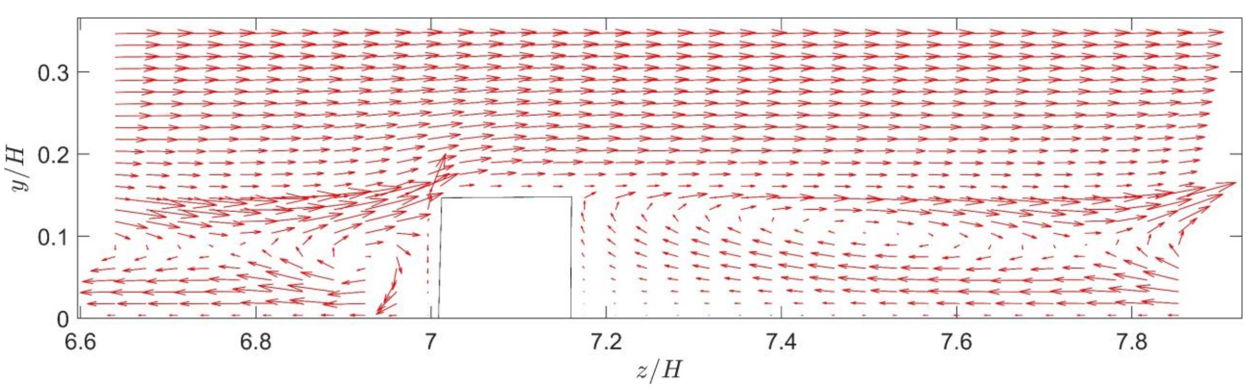

Figure 8 Velocity pattern near the rough-element (arrows not in scale).

The visible recirculation before and after the rough element has already been observed in previous work, as in [14, 24, 28], and it is supposed to highly interact with the main flow and exchange energy and momentum, enhancing diffusion phenomena. In addition, looking at the velocity profile in the wall-normal direction, it appears to be negative very near the flow, and then changes sign and increases until it matches the outer flow velocity. The change in the sign of the velocity will also cause a change in the sign of the shear stress, as can be seen in Fig. 9b, which is sometimes referred to as the point at which the wall is "perceived"; it is indeed common knowledge that roughness causes a shift in the velocity field and in the momentum equation, however, the value of this distance and how to predict it, is an actual research topic.

As can be seen in Fig.8, the flow is heavily disturbed and altered by the presence of the rough element, which is why in the following, we split the presentation of the results into four different regions of interest in the flow domain, which will be all indicated with capital letters in the subscript of quantities of interest: the first one is the top of the riblet, which will be indicated with "R" (riblet); the second one is the spacing between riblets, presented with "S" (spacing). The side-walls of the channels are also affected by the geometry of the bottom wall; thus we identify the left and right side-walls over the riblet with "RL" (riblet-left) and "RR (riblet-right), and the left and right side-wall in the spacing region as "SL" (spacing-left) and "SR" (spacing-right). Given this frame, Fig.9 presents the skin friction coefficient over these surfaces, evaluated as in Eq. (9-10).

DOI: 10.13009/EUCASS2023-507

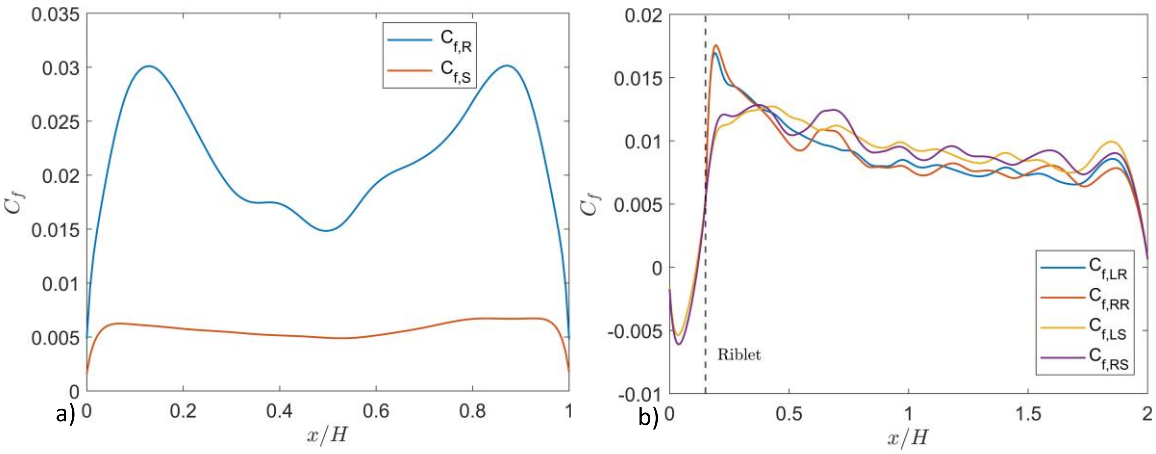

Figure 9 Skin friction coefficient on different walls of a duct with riblets

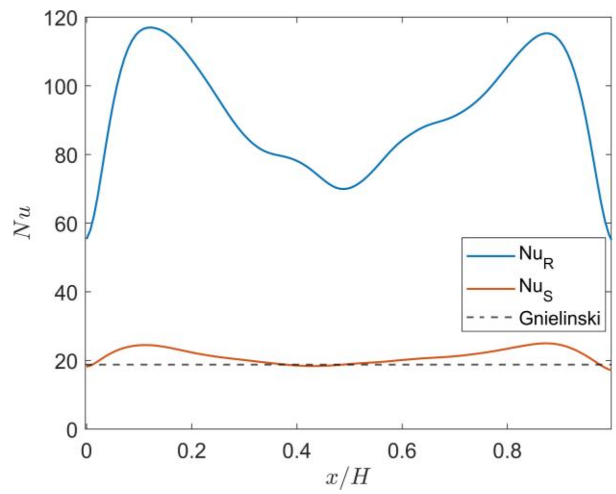

Figure 10 Nusselt number over the top of the riblet and over the spacing, in the rough duct simulation.

Fig.9a shows the skin friction coefficient on the top of the riblet (blue) and on the spacing wall (red); it is easily recognizable that over the riblet, the high gradient of velocity causes the friction coefficient to be several times larger with respect to the value which is found on the spacing-wall, that is much more similar to the value we found for the smooth wall, in Fig.4a. In addition, the side-walls present an overshoot in the skin friction coefficient for y-values which are close to the top of the riblet, as it can be seen in Fig.9b by the two curves named “LR” and “RR”; the other two curves, showing that the skin friction coefficient on the side-wall over the spacing region is flatter but still influenced; all the four curves converge to a similar value while moving away from the rough wall and getting closer to the smooth wall on the top. The same analysis is run for the heat transfer by using the Nusselt number, as it was done for the smooth duct. The results are shown in Fig.10, which shows once again a very similar profile as in Fig.9, in which the secondary motions of the fluid significantly enhance two peaks near the corners. As before, with the skin friction, the Nusselt number over the riblet results much higher than the value found on the spacing region, which is more similar to a smooth duct and in line with the prediction from Gnielinski correlation. Once again, we spend some lines to remark the importance of secondary flows occurring in rectangular cooling channels; in this case, as visible in Fig.9, two main currents are enhancing the diffusion mechanism, which are the sudden and steep rise of the flow right before the riblet, and the recirculation vortex created in the spacing region between different rough elements. These movements are much stronger than the recirculation vortices created by the anisotropy of the flow nearby the corners, which accounts for a magnitude in the order of 1-2% of the bulk velocity, as visible in Fig.5. Thus, in Fig.11 we present the cross-flow velocity over the spacing between riblets: three pairs of counter-rotating vortices are still visible near the top smooth

DOI: 10.13009/EUCASS2023-507

wall of the duct, as it was in the previous case, however their intensity is now small if compared to the recirculation occurring on the bottom wall, between the riblets.

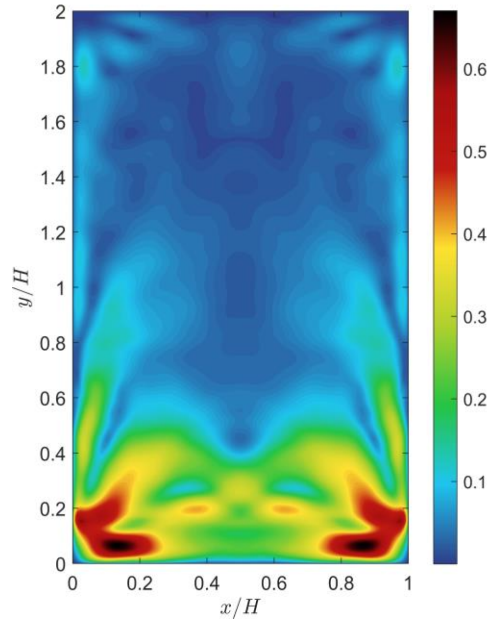

Figure 11 Cross-flow velocity $({U_x}^2 + {U_y}^2)^{0.5}$ *presented on a cross section of the smooth. duct*

The recirculation now has a predominant effect, which is almost one-order of magnitude larger than the secondary motions near the top corners; the recirculation adds up with the density gradient, which makes the flow move up, enhancing momentum and heat transfer and creating the peaks visible in Fig.9-10.
In conclusion, Fig.12 shows a comparison of the dimensionless temperature distribution across the channels for the same timestep in the two different simulations, with and without riblets: the dimensionless temperature is defined as $\theta = (T_H - T)/(T_H - T_C)$ where T_H is the hot temperature of the wall while T_C is the cold inlet temperature of the fluid.

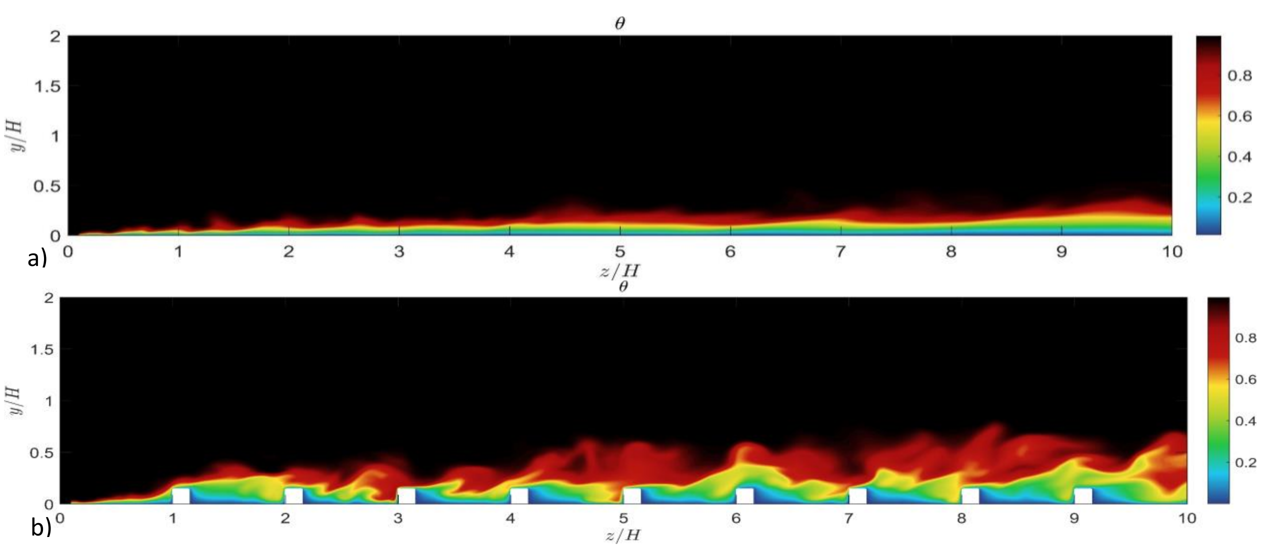

Figure 12 Dimensionless temperature at the same generic instant of time for a) the smooth duct simulation b) the riblet-duct simulation.

DOI: 10.13009/EUCASS2023-507

In Fig. 12, the enhancement of the diffusion mechanism created by the presence of rough elements is clearly visible: similar behavior is visible also if we look at the velocity components. The interaction of the rough surface and the flowing fluid creates ejections of hot fluid from the bottom wall up to the centerline of the duct, which of course, enhances mixing and thus the heat transfer process, locally and globally. These ejections of fluid were already presented in [28], where different shapes of the rough elements were compared to assess which one creates stronger fluctuations.
In order to try to determine the global increase in skin friction factor and Nusselt number which has been found in the simulation with riblets, with respect to the one with a smooth wall, we average the results, and compare in Tab.3. For the skin friction coefficient, due to the complex geometry, a more straightforward method can be employed, by evaluating the Darcy-Weisbach friction factor through the pressure variation across the duct, as in Eq. (10). For the Nusselt number instead, only the heated walls have to be considered: for the smooth wall, it is sufficient to average the wall shear stress over the perimeter of the section, Eq.(11), as it was done in [25]; for the riblet wall instead, an area-base average is needed, to account for the effect of both the surfaces of the riblet elements and the smooth spacing wall separating them, Eq.(12). Note that in Eq.(12), the first integral considers all the three surfaces of the riblet (front, top and back), however we shortened the equation for clarity.

$$\overline{\mathrm{C}}_{\mathrm{f}} = 4 f_{Darcy-Weisbach} = \frac{dp}{dx}\frac{2d_H}{\rho U^2} \tag{10}$$

$$\overline{\mathrm{Nu}_{\mathrm{smooth}}} = \frac{1}{H}\int_0^H Nu_{\mathrm{B}}\, dx \tag{11}$$

$$\overline{\mathrm{Nu}_{\mathrm{riblet}}} = \frac{1}{A_R + A_S}\left(\int_0^H \int_0^W Nu_{\mathrm{R}}\, dxdz + \int_0^H \int_0^S Nu_{\mathrm{S}}\, dxdz \right) \tag{12}$$

	C_f	Increase	Nu	Increase	RA	RA_{rough}/RA_{smooth}
Smooth	0.0073	-	15.99	-	0.907	-
Rough	0.0189	+159%	35.4	+121%	0.830	0.91

Since the obtained value for the Reynolds-Analogy factor is lower than 1, it confirms the expectations that the momentum loss over the rough surface is higher than the heat transfer enhancement obtained thanks to the same rough surface. However, due to the multiple averaging processes, this can only be considered an approximate global outcome, and a rigorous correlation can only be determined with more simulations and results.

6. Conclusion

Direct Numerical Simulations seem to be the most promising tool granting the accurate and detailed study of physical phenomena whose scale dimension would otherwise be very difficult to capture. The complex process of heat transfer over a rough wall, and more in general, the interaction of such a wall with a turbulent flow can be solved and understood through DNS because of the possibility to evaluate locally every property. However, the correct assumptions and simplifications are of paramount importance also when solving the N-S equations directly. Indeed, the choice of periodic boundary conditions on the side of the channel does not appear to be reasonable in liquid rocket engine application, where the accuracy needs to be the highest possible. The interaction between the turbulent flow and the side walls generates anisotropy in the Reynolds Stress tensor, which influences the flow pattern and, to a bigger extent, the overall performance in friction losses and heat transfer capabilities. Furthermore, a flat smooth wall cannot be assumed anymore, if additive manufacturing processes need to be considered, and the alteration caused by the wall profile has to be included in the simulation.
In this study, an ideal gas was simulated in a rectangular channel to show the effect of secondary motions on local friction and heat transfer phenomena, then compared against results over riblets. The increase of friction losses and heat transfer capabilities is pointed out and quantified with standard dimensionless numbers. The alteration of the flow pattern and the thermal boundary layer is visually presented, firstly to show the side-walls effects and the near-corner vortices and subsequently to highlight the effect of roughness protrusion. Even if discrete riblets are used, we believe that any shape and arrangement of rough elements would cause a similar effect, whose exact quantification would have to be simulated.

DOI: 10.13009/EUCASS2023-507

References

[1] J. Bons. 2005. A Critical Assessment of Reynolds Analogy for Turbine Flows. *Journal of Heat Transfer* 127, 5, 472–485.

[2] E. Brundrett and W Baines. 1964. The production and diffusion of vorticity in duct flows. *Journal of Fluid Mechanics* 19, 375–394.

[3] A. Busse and Oleksandr Zhdanoc. 2022. Direct numerical simulations of turbulent channel fow over ratchet roughness. *Flow, Turbulence and Combustion* 109, 1195–1213.

[4] Angela Busse, Mark Lutzner, and Neil Sandham. 2015. Direct numerical simulation of turbulent flow over a rough surface based on a surface scan. *Computers and fluids*, 129–147.

[5] James Cardillo, Chen, Yi, Araya, Guillermo, Jensen Newman, Kenneth Jansen, and Luciano Castillo. 2013. DNS of a turbulent boundary layer with surface roughness. *Journal of Fluid Mechanics* 729, 603–637.

[6] Giulo Croce, Paola D'Agaro, and Carlo Nonino. 2007. Three-dimensional roughness effect on microchannel heat transfer and pressure drop. *International Journal of Heat and Mass Transfer* 50, 5249, 5259.

[7] A. Favre. 1969. *Problem of Hydrodynamics and Continuum mechanics*, SIAM, Philadelphia.

[8] Karen Flack and Michael Schultz. 2010. Review of Hydraulic Roughness scales in the fully rough regime. *Journal of Fluids Engineering* 132.

[9] Pourya Forooghi, Alex Weidenlener, Franco Magagnato, Benjamin Böhm, Heiko Kubach, Thomas Koch, and Bettina Frohnapfel. 2018. DNS of momentum and heat transfer over rough surfaces based on realistic combustion chamber deposit geometries. *International Journal of Heat and Fluid Flow* 69, 83–94.

[10] Li Fuqiang, Li Zaizheng, Jing Kai, Wang Li, and Xiangwen, Zhang, Guozhu, Liu. 2018. Thermal Cracking of Endothermic Hydrocarbon Fuel in Regenerative Cooling Channels with Different Geometric Structures. *Energy Fuels* 32, 6524–6534.

[11] S. Gavrilakis. 1992. Numerical simulation of low-Reynolds-number turbulent flow through a straight square duct. *Journal of Fluid Mechanics* 244, 101–129.

[12] F. Gessner and J. Jones. 1965. On some aspetcts of fully developed turbulent. *Journal of Fluid Mechanics* 23, 689–713.

[13] T. O. Jelly, A. Ramani, B. Nugroho, N. Hutchins, and A. Busse. 2022. Impact of spanwise effective slope upon rough wall turbulent channel flow. *Journal of Fluid Mechanics* 951, 951.

[14] Javier Jimenez. 2004. Turbulent Flows over Rough Walls. *Annu. Rev. Fluid Mech.,* 36:173.

[15] R. H. Kraichnan. 1970. Diffusion by a random velocity field. *Physics of Fluids* 13, 22–31.

[16] S. Leonardi, Paolo Orlandi, and R. A. Antonia. 2007. Properties of d- and k-type roughness in a turbulent channel flow. *Physics of Fluids* 19, 125101.

[17] D. Martinez-Sanchis, A. Sternin, O. Haidn, and M. Tajmar. 2022. Turbulent combustion statistics in a diffusion flame for space propulsion applications. *Physics of Fluids* 34, 125115.

[18] D. Martinez-Sanchis, A. Sternin, T. Santese, and O. Haidn. 2023. The role of turbulence in the characteristic velocity and length of rocket combustors. *Aerospace and Technology* 134, 108158.

[19] D. Martinez-Sanchis, A. Sternin, D. Sternin, O. Haidn, and M. Tajmar. 2021. Analysis of periodic synthetic turbulence generation and development for direct numerical simulations applications. *Physics of Fluids* 33, 125130.

[20] D. Martinez-Sanchis, A. Sternin, Kenneth Tagscherer, D. Sternin, O. Haidn, and M. Tajmar. 2022. Interactions Between Flame Topology and Turbulent Transport in High-Pressure Premixed Combustion. *Flow, Turbulence and Combustion* 109, 813–838.

[21] Yutaka Miyake, Koichi Tsujimoto, and Yasuaki Agata. 2000. a DNS of a turbulent flow in a rough-wall channel using roughness element model. *JSME International Journal* 43, 2, 233–242.

[22] Yutaka Miyake, Koichi Tsujimoto, and Masaru Nakaji. 2001. Direct numerical simulation of rough-wall heat trasnfer in a turbulent channel flow. *International Journal of Heat and Fluid Flow* 22, 237–244.

[23] Davide Modesti, Sergio Pirozzoli, Paolo Orlandi, and Francesco Grasso. 2018. On the role of secondary motions in turbulent square duct flow. *Journal of Fluid Mechanics* 847.

DOI: 10.13009/EUCASS2023-507

[24] Yasutaka Nagano, Hirofumi Hattori, and Tomoya Houra. 2004. DNS of velocity and thermal fields in turbulent channel flow with transverse-rib roughness. *International Journal of Heat and Fluid Flow* 25, 25, 393–403.

[25] F. Nasuti, Andrea Torricelli, and Sergio Pirozzoli. 2021. Conjugate heat transfer analysis of rectangular cooling channels using modeled and direct numerical simulation of turbulence. *International Journal of Heat and Mass Transfer* 181, 121849.

[26] J. Nikuradse. 1950. *Laws of flow in rough pipes*. NACA, Washington.

[27] Paolo Orlandi and S. Leonardi. 2018. Direct numerical simulation of three-dimensional turbulent rough channels: parametriation and flow physics. *Journal of Fluid Mechanics* 606, 399–415.

[28] Paolo Orlandi, D. Sassun, and S. Leonardi. 2016. DNS of conjugate heat transfer in presence of rough surfaces. *International Journal of Heat and Mass Transfer* 100, 250–266.

[29] A. Pinelli, M. Uhlmann, A. Sekimoto, and G. Kawahara. 2010. Reynolds number dependence of mean flow structure in square duct turbulence. *Journal of Fluid Mechanics* 644, 107–122.

[30] Sergio Pirozzoli, Davide Modesti, Paolo Orlandi, and Francesco Grasso. 2018. Turbulence and secondary motions in square duct flow. *Journal of Fluid Mechanics* 840, 631–655.

[31] Stephan Pope. 2000. *Turbulent Flows*. Cambridge University Press, Cambridge.

[32] L. Prandtl. 1926. Ueber Die Ausgebildete Turbulenz. *Proceedings 2nd International Congress Applied Mechanics*, 62.

[33] W. M. Rohsenow, J. R. Hartnett, and Y. I. Cho. 1998. *Handbook of Heat Transfer*. McGraw-Hill, New York, USA.

[34] H. Schlichting. 1936. Experimentelle untersuchungen zum rauigkeitsproblem. *Ingenieur-Archiv* 7, 1–34.

[35] M. L. Shur, P. R. Spalart, M. K. Strelets, and A. K. Travin. 2014. Synthetic turbulence generators for RANS-LES interfaces in zonal simulations of aerodynamic and aeroacoustic problems. *Flow, Turbulence and Combustion* 93, 63–92.

[36] P. R. Spalart. 2000. Strategies for turbulence modelling and simulations. *International Journal of Heat and Fluid Flow* 21, 252–263.

[37] A. Sternin, D. Martinez-Sanchis, D. Sternin, and M. Tajmar. 2022. Characterisation and Design of Direct Numerical Simulations of Turbulent Statistically Planar Flames. *Aerospace* 9, 530.

[38] Manan Thakkar, A. Busse, and Neil Sandham. 2017. Surface correlations of hydrodynamic drag for transitionally rough engineering surfaces. *Journal of Turbulence* 18, 2, 138–169.

[39] M. Uhlmann, A. Pinelli, G. Kawahara, and A. Sekimoto. 2007. Marginally turbulent flow in a square duct. *Journal of Fluid Mechanics* 588, 153–162.

[40] R. Vinuesa, A. Noorani, A. Lozano-Duran, G. Khoury, P. Schlatter, P. Fischer, and H. Nagib. 2014. Aspect ratio effects in turbulent duct flows studied through direct numerical simulation. *Journal of Turbulence* 15, 10, 677–706.

[41] R. Vinuesa, C. Prus, P. Schlatter, and H. Nagib. 2016. Convergence of numerical simulations of turbulent wall-bounded flows and mean cross-flow structure of rectangular ducts. *Meccanica* 51, 3025–3042.

[42] H. Weller, G. Tabor, H. Jasak, and C. Fureby. 1998. A tensorial approach to computational continuum mechanics using object-oriented techniques. *COMPUTERS IN PHYSICS* 12, 6.

[43] Hao Zhang, Xavier Trias, Andrey Gorobets, Yanquiang Tan, and Assensi Oliva. 2015. Direct numerical simulation of a fully developed turbulent square duct flow up to $Re\tau = 1200$. *International Journal of Heat and Fluid Flow* 54, 258–267.

[44] Zuo-jin Zhu. 2009. Direct numerical simulation of turbulent flow in a straight square duct at Reynolds number 600*. *Journal of hydrodynamics* 21, 600–607.

[45] T. Zirwes, F. Zhang, J. Denev, P. Habisreuther, and H. Bockhorn. 2018. Automatedcode generation for maximizing performance of detailed chemistry calculationsin OpenFOAM. *High performance computing in science and engineering* 17, 189–204.

[46] T. Zirwes, F. Zhang, J. Denev, P. Habisreuther, H. Bockhorn, and D. Trimis. 2019. Improved vectorization for efficient chemistry computations in OpenFOAM for large scale combustion simulations. *High performance computing in science and engineering*, 209–224.

[47] T. Zirwes, F. Zhang, P. Habisreuther, J. Denev, H. Bockhorn, and D. Trimis. 2021. Implementation and validation of a computationally efficient DNS solver for reacting flows in OpenFOAM. *14th World Congress on ComputationalMechanics*.